Engineering Fracture Mechanics 141 (2015) 95–110

Contents lists available at ScienceDirect

Engineering Fracture Mechanics

journal homepage: www.elsevier.com/locate/engfracmech

Influence of static strain aging on the cleavage fracture of a C–Mn steel

A. Marais [a,b], M. Mazière [a,*], S. Forest [a], A. Parrot [b], P. Le Delliou [b]

[a] Mines ParisTech, Centre des Matériaux, CNRS UMR7633, BP 87, 91003 Evry Cedex, France
[b] EDF R&D/MMC, Site des Renardières, 77818 Moret s/Loing Cedex, France

ARTICLE INFO

Article history:
Received 17 June 2014
Received in revised form 21 January 2015
Accepted 30 April 2015
Available online 14 May 2015

Keywords:
Lüders band
Cleavage fracture
Charpy impact test
Piobert–Lüders
Numerical modeling

ABSTRACT

Recent advances in the constitutive modeling of strain aging effects in elastoviscoplasticity are used to predict the ductile-to-brittle transition curve for a C–Mn steel depending on pre-straining and heat treatment. The parameters of the Beremin model are identified from a large experimental basis of Charpy tests. 3D finite element simulations of Charpy V-notched specimens based on a constitutive model accounting for static strain aging, are performed for the first time to predict the fracture behavior of the pre-strained and aged material. The constitutive model includes the strain localization phenomena occurring in the notch due to Lüders effects. Good agreement between experiment and modeling is demonstrated. The introduction of kinematic hardening improves the prediction of the lower part of the ductile-to-brittle transition region. The proposed approach aims at optimizing pre-strain values and heat treatments for nuclear steels.

1. Introduction

The local approach to fracture is based, first, on a detailed metallurgical description of deformation and fracture mechanisms in metals and alloys, second, on a precise constitutive modeling of the elastoviscoplastic material behavior and, third, on coupled or uncoupled fracture criteria [13,39]. One major recent success of this approach has been to reconcile the interpretation in terms of fracture toughness of Charpy test results and fracture of Compact Tension specimens. In particular, some of the difficulties in the experimental and computational analysis of the Charpy test have been overcome in a series of works [45,43,44,27,26,52,53,47,49]. These works address in particular the Charpy tests at low temperature and the ductile-to-brittle transition in nuclear steels.

At low temperature and in the transition, cleavage is the main mechanism for brittle fracture in the ferritic nuclear steels, even though cleavage is always accompanied locally by intragranular plastic slip which becomes dominant with increasing temperature [41]. The fracture properties in the low temperature and transition regimes are statistical by nature due to the distribution of defects including inclusions or second phase in the material. They are very often satisfactorily described by means of the Beremin model which relates the Weibull distribution of fracture probability to a power-law distribution of defects and plasticity phenomena [10,11]. Such statistical fracture models can be applied to fracture mechanics samples like CT specimens [60], Charpy tests and structural components. They benefit from a detailed knowledge of the distribution of defects [51] and can incorporate the influence of loading rate [42]. More elaborate statistical models of fracture can be found in Bordet et al. [15].

* Corresponding author.
E-mail address: matthieu.maziere@mines-paristech.fr (M. Mazière).

http://dx.doi.org/10.1016/j.engfracmech.2015.04.035
0013-7944/

Nomenclature

CVN	Charpy V-notch impact energy (J)
$\boldsymbol{D}$	strain rate tensor
E_a	activation energy (eV)
$J_2(\boldsymbol{\sigma})$	von Mises equivalent stress
k_B	Boltzmann constant (1.38e−23 J/K)
$\boldsymbol{L}$	gradient of velocity field
m	Weibull exponent
p	cumulated plastic strain
$\dot{p}$	cumulated plastic strain rate (s^{-1})
P_r	failure probability
$\boldsymbol{Q}$	material rotation
t_a	current aging time (s)
t_{a0}	initial aging time (s)
T	temperature (K)
$\boldsymbol{T}$	Cauchy stress tensor (MPa)
V_a	activation volume
$\boldsymbol{X}$	kinematic hardening stress tensor (MPa)
$\boldsymbol{\alpha}$	hardening internal variable
$\boldsymbol{\Lambda}$	tensor of elastic moduli (MPa)
ρ	current dislocation density (m^{-2})
ρ_0	initial dislocation density (m^{-2})
$\rho_{5\%}$	dislocation density for the 5% pre-strained state (m^{-2})
$\dot{\varepsilon}$	observer invariant strain rate tensor
$\dot{\varepsilon}_e$	elastic strain rate tensor
$\dot{\varepsilon}_p$	plastic strain rate tensor
$\boldsymbol{\sigma}$	observer invariant stress tensor (MPa)
σ_w	Weibull stress (MPa)
σ_I	maximum principal stress (MPa)

Strain aging characterizes the mechanical behavior of most nuclear steels due to the interaction of solute atoms present in the alloys and dislocations [16,54]. Static strain aging (SSA) is observed at lower temperature for instance in the form of Lüders peak stress and plateau accompanied by the propagation of plastic strain localization bands along the sample or at geometrical singularities in structural components. In service conditions at higher temperatures very often correspond to the domain of dynamic strain aging (DSA) which can be associated with the Portevin–Le Chatelier effect, i.e. the formation and propagation of plastic strain rate localization bands. In the context of fracture mechanics, the Lüders and Portevin–Le Chatelier effects are usually not taken into account in the computational modeling of fracture processes. Heuristic rules are chosen to fix the initial yield stress and the strain localization phenomena are not incorporated. DSA effects are smoothed out and the possible negative strain rate sensitivity is usually not accounted for. However, reliable constitutive equations have been available for more than ten years that include the strain aging effects in the elastoviscoplastic material laws. The associated instabilities have been investigated by Mesarovic [35], Benallal [6], and Benallal et al. [8,7]. Finite element (FE) simulations of plastic strain and strain rate phenomena in tensile or fracture mechanics samples were first performed by Zhang et al. [63] and Graff et al. [20,21] for aluminum alloys and mild steel. The constitutive models are mature for full 3D implicit FE computations and detailed comparison with experimental data like strain field measurements, as done for the Lüders effect by Ballarin et al. [4,3], Hallai and Kyriakides [23,24], Marais et al. [30], and Hallai and Kyriakides [25]. The simulations include the local stress and strain rate concentration induced by the development of spatio-temporal instabilities.

The importance of strain aging on the fracture properties of engineering steels is well recognized in the mechanical metallurgy community. DSA effects in C–Mn steels were investigated by Wagner et al. [55–57], for CT specimens but also in welded zones, taking heat treatments into account. More recent works are based on constitutive modeling of dynamic strain aging and explicit modeling of PLC bands in notched and CT specimens [5,58,59,9]. In the latter work, it was shown that a reduction of ductility is observed in the DSA domain of material behavior. The impact of static strain aging on fracture toughness was first addressed in Houssin et al. [28] and Amar and Pineau [1] in the case of CT specimens. Recent contributions make use of Zhang and McCormick's model for the computation of the elastoviscoplastic response of a CT specimen, including a detailed 3D analysis of strain localization phenomena at the crack tip by Wenman and Chard-Tuckey [61].

What is missing in the literature is the direct use of strain aging constitutive models for the prediction of brittle-to ductile transition curves. This is the objective of the present work in the case of a C–Mn nuclear steel. For that purpose, the proposed methodology combines the tools of local approach to fracture as presented in Pineau [40] and the detailed elastoviscoplastic

constitutive modeling of static strain aging in this alloy, as established by Marais et al. [30]. Novel aspects of the work include the direct simulation of Charpy tests at different temperatures and the identification of a statistical fracture model delivering the ductile-to-brittle transition curve as a function of SSA induced by pre-straining, heat treatment and loading path history.

The outline of the paper is as follows. The experimental methods and mechanical test results are presented in Section 2. They include the Charpy V-notch (CVN) test results for three different material strain aging states over a range of temperatures from −100 °C to 100 °C. The equations and material parameters of the constitutive model accounting for strain aging dependent elastoviscoplasticity are given in Section 3. In the same section, the finite element results of the CVN simulations are used to identify the Beremin model for the base material state. Predictions of the constitutive and fracture models are then provided for other aging states and compared to experimental results. The influence of the Bauschinger effect on CVN predictions at the lower part of the ductile-to-brittle transition region is also investigated. The results are finally discussed in Section 4.

2. Experimental procedure

2.1. Material

All experiments were conducted on a C–Mn steel used for pipes of the secondary circuit in power plants, called here A42, whose chemical composition is given in Table 1. This alloy is very sensitive to strain aging due to the small *Al* content. The material is extracted from a seamless secondary coolant pipe obtained by a circular rolling process. The microstructure is composed of ferrite and pearlite in alternate bands along planes parallel to the axial and circumferential directions. The crystallographic texture was not analyzed. However, the cross-section of cylindrical tensile specimens remains circular up to fracture strain. This indicates a quasi-isotropic mechanical behavior at least in the long and short transverse plane. By extension, we considered the mechanical behavior as fully isotropic, weakly affected by the morphological texture, nor by the crystallographic texture, thus following Belotteau et al. [5].

The mechanical behavior of this material under simple tension has been investigated in a previous article [30]. This contribution was devoted to the experimental analysis and modeling of the stress peak and Lüders plateau experimentally observed at several temperatures from −150 °C to 20 °C. The tensile curves are recalled in Fig. 1 and show the temperature dependence of peak stress and Lüders plateau. The constitutive model identified in the latter work is used in the numerical simulations of the present paper.

2.2. Testing conditions

Standard Charpy V-notch specimens with a (10×10) mm^2 section, a central 45° V-notch of 2 mm depth and a 0.25 mm notch root radius were tested in accordance with the French standard for impact testing of Charpy specimens (NF EN 10045-1) on an instrumented 450 J capacity impact tester. The notch plane is perpendicular to the transverse direction *T* and crack growth direction parallel to the longitudinal direction *L* of the plate. The acquisition frequency is 250 kHz. These impact tests were carried out with an impact velocity equal to 5 m s^{-1}. The testing temperature varies over the range −100 °C to 80 °C.

Table 1
Chemical composition (weight percent) of the Carbon Manganese steel A42.

Steel	C	N	Al	Si	P	S	V	Cr	Mn	Ni	Cu	Nb	Mo	Sn
A42	0.15	0.004	0.019	0.19	0.034	0.021	<0.002	0.034	0.73	0.05	0.041	<0.002	0.006	0.003

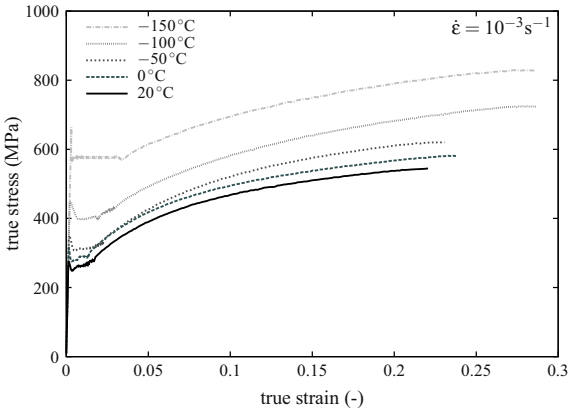

Fig. 1. Experimental tensile curves for different temperature from Marais et al. [30]. A stress peak and Lüders plateau is evidenced at all temperatures.

Table 2
Number of specimens tested for each state and each temperature. Dispersion of results is determined using the numerous experiments at −20 °C.

Charpy impact tests	Temperature (°C)							
	−100	−50	−20	0	20	40	60	80
BS	2	2	20	3	3	×	2	2
5% pre-strained	2	2	18	3	5	2	2	2
5% pre-strained + aged	2	2	18	3	5	2	2	2

Three different states for the C–Mn steel were tested using the same procedure. The first state is denoted "BS" and corresponds to the as-received material without any additional heat treatment or pre-straining. The second material state denoted "5% pre-strained" was designed in order to study the influence of pre-straining on fracture. Numerous Charpy specimens were then cut in a 5% pre-strained 710 mm × 40 mm × 40 mm bar. This pre-straining was carried out along the transverse orientation (T) of the plate. The third material state is denoted "5% pre-strained + aged". Half of the specimens cut from the pre-strained bar were subjected to an aging heat treatment (30 min at 250 °C) in order to generate this last material state. The influence of the aging heat treatment on fracture is investigated by comparison of these specimens with the "5% pre-strained" ones. The number of Charpy tests performed for each material state and each temperature is given in Table 2.

2.3. Fracture tests

Representative Charpy experimental load displacement curves for the three aforementioned material states are shown in Fig. 2 for temperature T = 0 °C and T = 20 °C. The load level is higher for the 5% pre-strained and 5% pre-strained + aged states than for the base state because of hardening. The height of the second peak is also higher for the 5% pre-strained + aged than for the 5% pre-strained as expected due to the aging effect. At both temperatures, the energy required to break the specimens seems to be smaller in the 5% pre-strained + aged state than for the 5% pre-strained, than for the state BS.

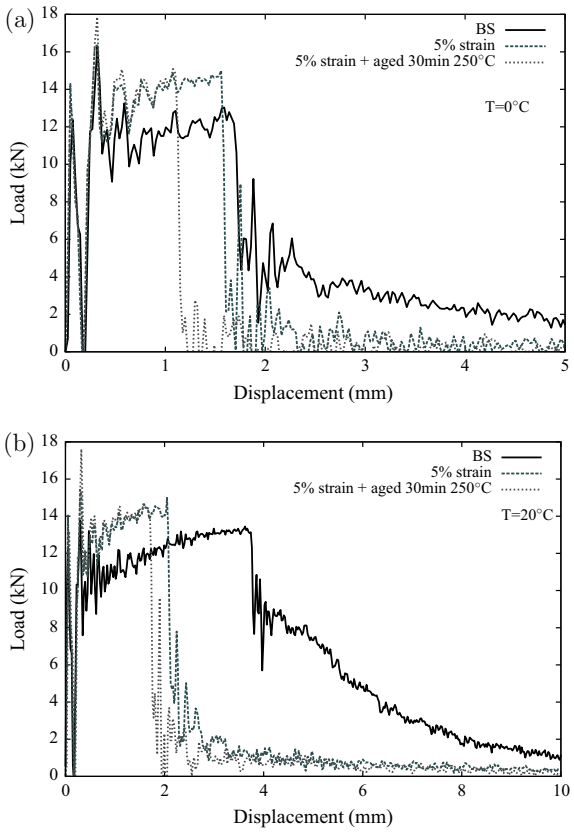

Fig. 2. Load–displacement curves for Charpy test on the 3 material states: (a) at 0 °C and (b) at 20 °C.

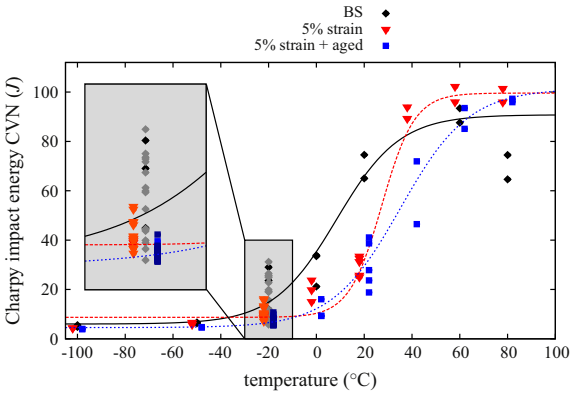

Fig. 3. Charpy fracture energy transition curves of C–Mn steel for Charpy specimens tested at different states, BS, 5% pre-strained and 5% pre-strained + aged.

Table 3
Parameters of the CVN energy fitting function and index TK_7 for different material states.

Material state	A (J)	B (J)	T_0 (°C)	C	TK_7 (°C)
BS	48.4	42.4	8.67	30.29	13.2
5% pre-strained	54.2	45.4	27.39	13.67	28
5% pre-strained + aged	52.96	48.4	35.17	28.65	37

The material state significantly affects the dependence of experimental Charpy impact energies on temperature, as shown in Fig. 3. The energies of the Charpy V-notch (CVN) tests obtained from Table 2 were fitted for each state with an hyperbolic tangent function of temperature as proposed by Oldfield [38]:

$$\mathrm{CVN}(J) = A + B\tanh\left((T - T_0)/C\right) \tag{1}$$

Parameters A, B, C, T_0 of Eq. (1) are given in Table 3. For each condition, only the three first experiments were taken into account at -20 °C in the parameter identification in order to give to this temperature the same weight as the other ones. The temperature denoted TK_7 is also reported in Table 3 since this temperature is currently used in Charpy impact tests analysis. It is defined as the temperature for which the CVN energy is 56 J ($\mathrm{CVN}/S_r = 7$ da J/cm^2 with S_r the fracture surface, $S_r = 0.8$ cm^2).

The ductile-to-brittle transition is shifted towards higher temperatures for the 5% pre-strained state. This shift is increased for the 5% pre-strained + aged state, as shown by the corresponding value of the TK_7 parameter from Table 3.

The scatter of CVN energies at -20 °C for the three material states is plotted in Fig. 4 for the three material states. The mean value of this energy decreases from 18.1 J to 10.5 J for the base and 5% pre-strained states respectively, and to 7.29 J for the 5% pre-strained + aged state. This result is consistent with the transition curves plotted in Fig. 3. A large number of experiments were carried out at this temperature (almost 20 for each state) so as to obtain a reliable estimation of the scatter which is high at this temperature. The standard deviation follows the same trend as the mean value and decreases from 7.8 J for the based state to 2.57 J for the 5% pre-strained state and to 1.43 J for the 5% pre-strained + aged state. The scatter of experimental results is therefore significantly affected by the pre-strain and by the aging treatment.

Based on all these results (Figs. 3 and 4), it can be concluded that at -20 °C, the material in its as-received state still is in the ductile-to-brittle transition. In contrast at the same temperature for the two other conditions, the material is below the transition in the brittle fracture domain and the ductile-to-brittle transition is then shifted towards higher temperatures. The shift in the transition domain is emphasized by the aging treatment applied to the prestrained material, and can lead to unexpected failure of the material.

3. Numerical modeling

3.1. Constitutive equations

The simulation of strain aging requires a suitable choice of an elastoviscoplasticity model including the physical mechanisms of pinning and unpinning of dislocations. The model retained in this work and initially proposed by Kubin, Estrin, McCormick [29,34] is based on the introduction of an internal variable t_a called aging time with a suited evolution law coupled with plastic flow. It has been implemented in the finite element code Zset and used in several previous studies

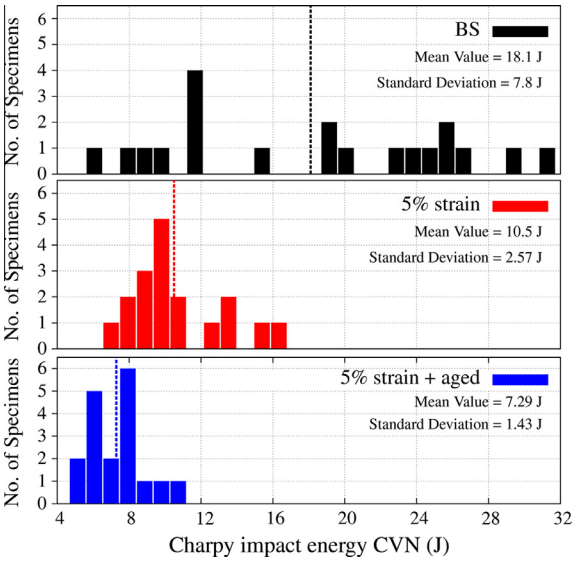

Fig. 4. CVN energies at −20 °C (scatter temperature) for the 3 material states, including the corresponding average values and standard deviations.

[5,31,58,32]. For more details about the model, its implementation and the identification process, the reader is referred to a previous article by the same authors [30].

A finite strain formulation for isotropic nonlinear material behavior is adopted in this work based on the concept of local objective frame as proposed in Sidoroff and Dogui [48], Bertram [12], and Besson et al. [14]. Observer invariant stress and strain rate measures $\boldsymbol{\sigma}$ and $\dot{\varepsilon}$ are defined by transport of the Cauchy stress tensor $\boldsymbol{T}$ and the strain rate tensor $\boldsymbol{D}$ into the corotational frame characterized by the rotation $\underset{\sim}{\boldsymbol{Q}}(\underline{\boldsymbol{x}}, t)$. This change of frame takes place at each material point:

$$\begin{cases} \underset{\sim}{\boldsymbol{\sigma}} = \underset{\sim}{\boldsymbol{Q}} \cdot \underset{\sim}{\boldsymbol{T}} \cdot \underset{\sim}{\boldsymbol{Q}}^T \\ \underset{\sim}{\dot{\varepsilon}} = \underset{\sim}{\boldsymbol{Q}} \cdot \underset{\sim}{\boldsymbol{D}} \cdot \underset{\sim}{\boldsymbol{Q}}^T \\ \underset{\sim}{\boldsymbol{Q}} \text{ such as } \dot{\underset{\sim}{\boldsymbol{Q}}}^T \cdot \underset{\sim}{\boldsymbol{Q}} = \underset{\sim}{\boldsymbol{\Omega}} \text{ (corotational)} \end{cases} \tag{2}$$

where $\underset{\sim}{\boldsymbol{\Omega}}$ is the skew-symmetric part of the gradient $\underset{\sim}{\boldsymbol{L}}$ of the velocity field, and $\underset{\sim}{\boldsymbol{D}}$ its symmetric part [48,14].

The strain rate tensor $\underset{\sim}{\dot{\varepsilon}}$ is split into elastic and plastic contributions, the evolution of the latter being given by the plastic flow rule. The stress is computed from the elastic strain $\underset{\sim}{\varepsilon_e}$ through Hooke's law:

$$\underset{\sim}{\dot{\varepsilon}} = \underset{\sim}{\dot{\varepsilon}_e} + \underset{\sim}{\dot{\varepsilon}_p}, \quad \underset{\sim}{\boldsymbol{\sigma}} = \underset{\approx}{\boldsymbol{\Lambda}} : \underset{\sim}{\varepsilon_e} \tag{3}$$

The plastic strain is computed from the normality rule

$$\underset{\sim}{\dot{\varepsilon}_p} = \dot{p}\, \underset{\sim}{\boldsymbol{n}}, \quad \underset{\sim}{\boldsymbol{n}} = \frac{\partial f}{\partial \underset{\sim}{\boldsymbol{\sigma}}} \tag{4}$$

and the equivalent plastic strain rate $\dot{p}$ follows a thermal activation law defined as:

$$\dot{p} = \dot{p}_0 \sinh\left(\frac{\langle f \rangle}{K}\right) = \dot{\varepsilon}_0 \exp\left(-\frac{E_a}{k_B T}\right) \sinh\left(\frac{V_a \left\langle f\left(\underset{\sim}{\boldsymbol{\sigma}}, \rho, t_a\right)\right\rangle}{k_B T}\right) \tag{5}$$

where T is the temperature in Kelvin, k_B is the Boltzmann constant and $\dot{\varepsilon}_0, E_a$ and V_a respectively are a strain rate parameter, the activation energy and the activation volume of the physical mechanisms of plasticity.

The function f in Eq. (4) is the yield function which is based on a von Mises criterion with isotropic hardening:

$$f\left(\underset{\sim}{\boldsymbol{\sigma}}, \rho, t_a\right) = J_2(\underset{\sim}{\boldsymbol{\sigma}}) - R(\rho) - R_a(t_a) \tag{6}$$

$$R(\rho) = \sigma_0 + \gamma \mu b \sqrt{\rho}, \quad \dot{\rho} = A\left(1 - \frac{\rho}{B}\right)\dot{p}, \quad R_0 = \sigma_0 + \gamma \mu b \sqrt{\rho_0} \tag{7}$$

where $J_2(\underset{\sim}{\boldsymbol{\sigma}})$ is the von Mises equivalent stress. The dislocation density ρ is introduced in the model (initial value ρ_0). The classical strain hardening is given by the term $R(\rho)$ which follows the evolution law defined in Eq. (7), the multiplication and dynamic recovery parameters characterizing the evolution law of this variable being A and B, respectively. The dislocation density evolution rule is driven by the cumulative plastic strain rate $\dot{p}$, as done for instance in Fressengeas et al. [19]. The yield stress R_0 is the "virtual" initial microscopic yield stress that would be measured in the same steel in the absence of static strain aging.

The second contribution to the yield stress, $R_a(t_a)$, is due to strain aging, following [63,20,31]. It depends on an additional internal variable t_a called the aging time, and takes the form

$$R_a(t_a) = P_1 C_s(t_a), \quad \text{with} \quad C_s = 1 - \exp\left[-\left(\frac{t_a}{t_0}\right)^n\right] \tag{8}$$

$$\dot{t}_a = 1 - \frac{t_a \dot{p}}{\omega} \tag{9}$$

The strain aging term R_a is proportional to the variable C_s that is related to the over-concentration of solute atoms around pinned dislocations. This variable increases with the aging time t_a, the condition corresponding to fully pinned dislocations being given by $C_s = 1$. The unpinned state corresponds to $C_s = 0$. The parameter P_1 corresponds to the maximal additional stress needed to switch from unpinned to pinned conditions. The parameter t_0 and the power n control the kinetics of the pinning and unpinning processes. Another parameter labeled ω appears in the evolution law of the aging time. It is related to the incremental strain resulting from the freeing of unpinned dislocations.

The identification of this model over a large range of temperatures (from −150 °C up to 20 °C) and strain rate (from 1e−5 s^{-1} up to 1e−1 s^{-1}) was carried out using numerous simple tensile experiments as described in Marais et al. [30]. The identification procedure which takes into account the characteristics of the Lüders phenomenon is not recalled. The parameters for the five temperatures of interest in the present work are given in Table 4.

3.2. Cleavage fracture prediction

The constitutive material model is associated with a non-coupled brittle (cleavage) fracture model according to Mudry [36,37], Beremin [11], and François et al. [18], which is one of the most popular local approach models in this area, denoted Beremin model. It is based on the hypothesis of a (temperature-independent) critical cleavage stress, and on weakest link theory. The failure probability P_r is given as:

$$P_r = 1 - \exp\left[-\left(\frac{\sigma_w}{\sigma_u}\right)^m\right] \tag{10}$$

with σ_w, the "Weibull stress"

$$\sigma_w = \sqrt[m]{\int_{Vp} \max_{0\leqslant\tau\leqslant t}(\sigma_I^\tau)^m \frac{dV}{V_0}} \tag{11}$$

where σ_I^τ denotes the maximum principal stress (here defined as its maximum value with time), m the Weibull exponent which is related to the scatter in the distribution of defects responsible for fracture, and σ_u is closely linked to the intrinsic cleavage stress. The integral denotes the summation of σ_I^τ over the entire plastified volume V_p of the structure (i.e., all

Table 4
Constitutive parameters describing elasticity, viscoplasticity, hardening and aging.

T (°C)	**−150**	**−100**	**−50**	**0**	**20**
E (GPa)	214	220	219	221	218
ν	0.3	0.3	0.3	0.3	0.3
R_0 (MPa)	360	225	145	147	150
σ_0 (MPa)	340	205	124	126	130
ρ_0 (m^{-2})	1e13	1e13	1e13	1e13	1e13
A (m^{-2})	2.26e16	3.5e16	4.15e16	3.87e16	3.09e16
B (m^{-2})	1.47e16	9.2e15	8.08e15	5.12e15	5.11e15
$\dot{\varepsilon}_0$ (s^{-1})	1e−7	1e−7	1e−7	1e−7	1e−7
E_a (eV)	0.0022	0.0022	0.0022	0.0022	0.0022
V_a (b^3)	27	59	90	121	133
P_1 (MPa)	396.6	316	285	220	183.2
t_0 (s)	3.49e13	1.24e12	2.81e8	1.01e5	1.59e4
t_{a0} (s)	3.49e13	1.24e12	2.81e8	1.01e5	1.59e4
ω	5e−4	5e−4	5e−4	5e−4	5e−4
n	0.137	0.144	0.199	0.306	0.334

Bold was a way to highlight the temperatures.

elements that have undergone plastic deformation), since plastic deformation is a necessary precursor to slip-induced cleavage (e.g., by a dislocation pile-up mechanism). Two independent parameters are required: m and $V_0\sigma_u^m$.

The fracture criterion is thus based on one mechanical variable, i.e., namely the maximum positive principal stress. Fracture is assumed to occur as soon as this quantity reaches a critical value for unstable propagation of a cleavage micro-crack. There are some guidelines for the choice of V_0. On the one hand, V_0 should be large enough in order to allow for the presence of a critical defect. On the other hand, V_0 should be small enough in order to resolve strong stress gradients, as they occur ahead of a crack tip. In "local" FEM computations (i.e. if no averaging over several finite elements is carried out) the size of V_0 is related to the mesh size, see [13]. Thus the choice of the mesh size is important for ductile crack growth modeling, as well as for cleavage fracture modeling. V_0 was chosen equal to $(50\ \mu m)^3$ [18].

The model parameters σ_u and m are first identified using Charpy impact tested at temperature $-20\ ^\circ C$ for the base state. Twenty tests were performed. The parameters are identified using an automatic identification procedure which minimizes the quadratic difference between the theoretical and experimental failure probabilities [53] described briefly below:

1. For each Charpy experiment, the CVN energy is computed from the load vs. displacement curves, and experiments are sorted in ascending order.
2. The failure probability associated to the stress reached by specimen at rank i is evaluated using the following formula: $P_{f,i}^{exp} = \frac{i}{N+1}$ where N is the total number of specimens and $i = 1, \ldots, N$ the rank of the specimen.
3. The displacement (of the striker) at failure is evaluated for each experiment.
4. A finite element simulation of the Charpy test at $-20\ ^\circ C$ is carried out beyond the maximal experimental displacement reached by the 20 experiments. The corresponding finite element model is detailed in Section 3.3.
5. For each calculation step corresponding to an experimental failure displacement, the experimental Weibull stress σ_w^{exp} is estimated from the finite element results.
6. The experimental evolution of $P_{f,i}^{exp}$ as a function of σ_w^{exp} is compared to the Beremin model $P_f^{mod}(\sigma_w)$ given by Eq. (10).
7. If both evolutions are in agreement, the iterative process is stopped. Otherwise, m and σ_u are modified and the algorithm goes to step 5.

Experimental and theoretical failure probabilities are compared in Fig. 5 as functions of the computed Weibull stress. In this figure, a good agreement between experimental and theoretical values is observed when adopting the following values for the Weibull parameters: $m = 23$ and $\sigma_u = 1654$ MPa. The value found for the Weibull shape factor m is close to those reported in the original Beremin work on another pressure vessel steel [11], or in a more recent article on ferritic steels [2].

3.3. Modeling of the Charpy transition curve for the base state

In order to understand the effect of strain and aging on the transition curve, finite element simulations of the Charpy impact test were carried out using the finite element software Zset [62]. All the simulations were performed on the 2D mesh presented in Fig. 6 using plane strain formulation. Some simulations using plane stress formulation or full 3D mesh have also been carried out. The global force vs. displacement curve for plane strain and plane stress formulation were found to be located respectively above and below that of the 3D curve. However when the evolution of the maximum principal stress is plotted beyond notch tip, results for plane strain and 3D simulation are very close and different from the corresponding plane stress result. Since this variable is the most important one for the application of the Beremin model presented in Section 3.2, the plane strain formulation is selected for this study, in agreement with recommendations from Rossoll et al. [44].

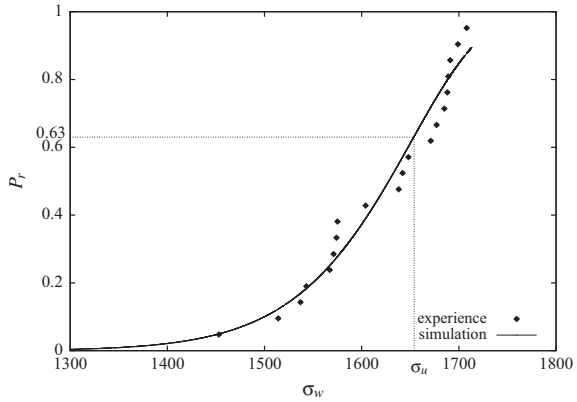

Fig. 5. Identification of the Beremin model parameters for brittle fracture of the C–Mn steel.

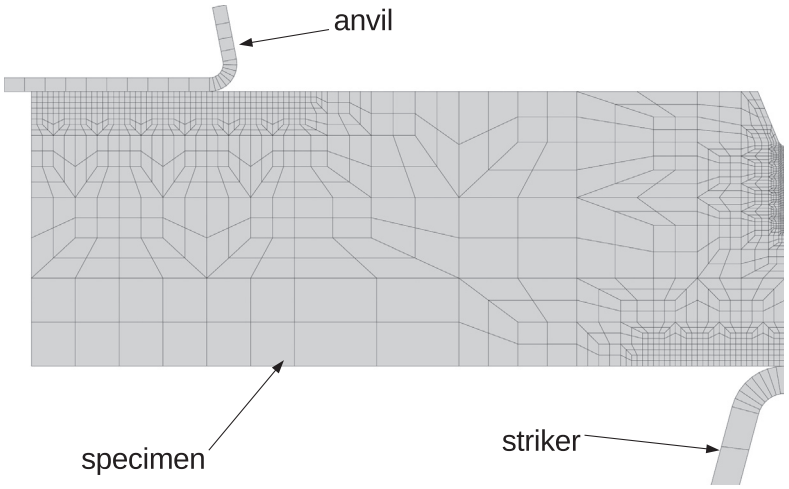

Fig. 6. Two-dimensional finite element mesh of the Charpy specimen, including the anvil and the striker parts. The mesh size beyond notch tip is 60 μm.

The finite elements chosen were four node linear square elements with selective integration [14] in the contact zones and eight node quadratic squares in the rest of the specimen, using a continuous interface condition between both zones. The influence of mesh size was investigated in order to reach convergence of the maximal principal stress beyond notch tip. As a result of this analysis, the element size was fixed equal to 60 μm.

The boundary conditions of the finite element simulations are the following. A velocity of $V = 5$ m s^{-1} is prescribed to the striker, while the anvil remains fixed. The friction coefficient between these two parts and the specimen is equal to 0.1. This coefficient is particularly significant in case of ductile failure propagation (i.e. for high level of CVN energy), but less important in our case where the lower part of the ductile-to-brittle transition is investigated. The striker and the anvil are modeled as rigid bodies in order to improve the convergence of the contact algorithm. It has been shown in Rossoll et al. [44] that accounting for the elasticity of these parts does not modify significantly the results.

The simulations were carried out using a quasi-static isothermal formulation as suggested in Rossoll et al. [44]. This point may be reconsidered in future work especially at low temperature for which inertial effects may play a more significant role.

The material model described in Section 3.1 was used at 6 different temperatures (−150 °C, −100 °C, −50 °C, −20 °C, 0 °C, 20 °C) to simulate the Charpy impact tests using the numerical model presented above. At each temperature, the CVN energies for a fracture probability of 10%, 50%, and 90% are evaluated using the area under the force vs. displacement curve at the corresponding calculation steps. These steps are defined after applying the Beremin model with the parameters identified in Section 3.2.

The results are plotted in Fig. 7 giving the energy at 10%, 50%, and 90% as a function of temperature. At −20 °C, the numerical prediction is in exact agreement with experimental results due to the fact that the Beremin model parameters were identified at this temperature for this material state. At all other temperatures the experimental points remain inside the 10–90% bounds, even at higher temperature (20 °C), thus showing the predictive capabilities of the model. Note that at this temperature the fracture of the material is probably not fully brittle and that the Beremin model should be associated with a

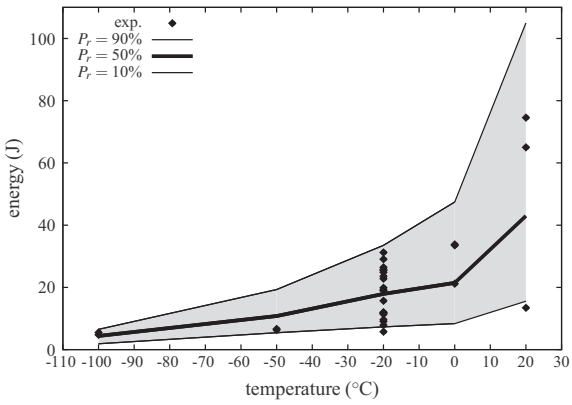

Fig. 7. Prediction of the Charpy transition curve at cleavage initiation assuming a constant value for σ_u for the base state (BS).

coupled ductile damage model as done in some previous work [53]. However, in this study we are focusing on the influence of pre-straining and aging on the lower part of the ductile-to-brittle transition curve.

The parameter σ_u remains constant for all temperatures. The predictions of the model can be improved if a temperature dependence of σ_u is introduced. In this study, the Beremin parameter values are kept constant for all temperatures and all material states in order to highlight the ability of the model to describe the observed phenomena.

3.4. Simulation of the Charpy transition curve for the 5% pre-strained and 5% pre-strained + aged states

The Charpy experiments for the 5% pre-strained state were simulated by changing, in the material model, the initial values of the internal variables, namely the dislocation density ρ and the aging time t_a. The initial values to be prescribed were calculated after simulating a tensile test up to 5% (see [30] for details). They are given as $\rho_{5\%}$ and t_{a0} in Fig. 9 and can be compared to the base state values.

The same approach was applied to the 5% pre-strained + aged state simulation of Charpy impact tests. The initial value of ρ is the same as for the 5% pre-strained state based on the assumption that the aging treatment (30 min at 250 °C) does not modify the dislocation density. This assumption could be reconsidered accounting for the influence of static recovery due to time driven and thermally activated dislocation annihilation. In order to evaluate the impact of the aging treatment at 5% pre-strained on the mechanical behavior and particularly of the aging part of this model related to the internal variable t_a, an original specific experiment was performed. It is presented in Fig. 8.

The strain stress curve denoted "ST" on this figure is a simple tensile experiment from Marais et al. [30] at 20 °C and a prescribed strain rate $1 \cdot e{-}3\ s^{-1}$. The second curve denoted "ST 0–5%/30 min at 250 °C/ ST 5–10%" is the mechanical response of a specimen made of the same material with slightly different dimensions submitted to the following thermo-mechanical path:

- Simple tension up to 5% of global strain at 20 °C and a prescribed strain rate $1 \cdot e{-}3\ s^{-1}$.
- Unloading to zero force.
- Aging treatment 30 min at 250 °C.
- Reloading up to 10% of global strain at 20 °C and a prescribed strain rate $1 \cdot e{-}3\ s^{-1}$.

Both curves slightly differ in the first stage before 5% because of the difference of specimen dimension and experimental scatter. After 5% the aging treatment gives rise to a stress peak and a Lüders plateau. After the Lüders stage, the curve is parallel but not superimposed to the ST curve. This means that the unpinning did not free all dislocations so that the stress level is higher. Note that this feature, although frequent in steels, is not reproduced by the constitutive model of this work. The precise modeling of the amount of unpinning remains an open question from the constitutive modeling point of view. Since the size of the stress peak is close to the initial one, the initial value of t_a for the 5% pre-strained + aged state is then prescribed at each temperature at the same value as for the base state (see Fig. 9).

The numerical procedure of Section 3.3 has been applied to the modified material behaviors presented in Fig. 9. For both states the Charpy experiments were simulated at 6 different temperatures (−150 °C, −100 °C, −50 °C, −20 °C, 0 °C, 20 °C). The Beremin model was applied to evaluate the CVN energy vs. temperature curves for three fracture probability values (10%, 50%, and 90%). The Beremin parameters m and σ_u identified at −20 °C for the base state were kept constant in order to highlight the influence of strain and aging on fracture through the material behavior. The results of this analysis are plotted in Fig. 10. The predictions for both states are in good agreement with the corresponding experimental results since

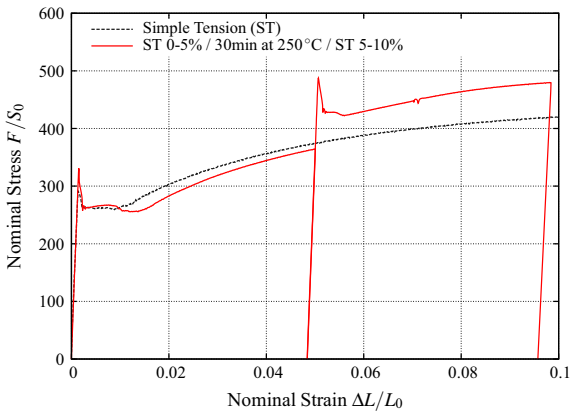

Fig. 8. Comparison between a monotonic simple tensile experiment at 20 °C and a prescribed strain rate $1 \cdot e{-}3\ s^{-1}$, and the same experiment interrupted at 5% of global strain to carry out an aging treatment of 30 min at 250 °C at zero force. The aging treatment gives rise to a Lüders peak and plateau when the specimen is reloaded.

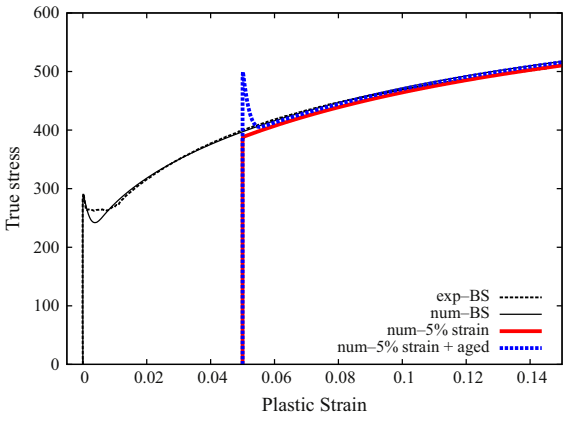

Initial values	BS	5% pre-strained	5% pre-strained + aged
$\rho_0, \rho_{5\%}$ (m^{-2})	1.e13	1.3e15	1.3e15
t_{a0} (s)	1.6e4	$\simeq 0$	1.6e4

Fig. 9. Initial values of the internal variables for the three material states at 20 °C. ρ_0 controls the level of prestraining while t_{a0} sets the level of dislocation pinning and allows to switch between aged and non-aged states. The stress vs. plastic strain responses of the model on a material point associated with each initial condition are plotted above the table.

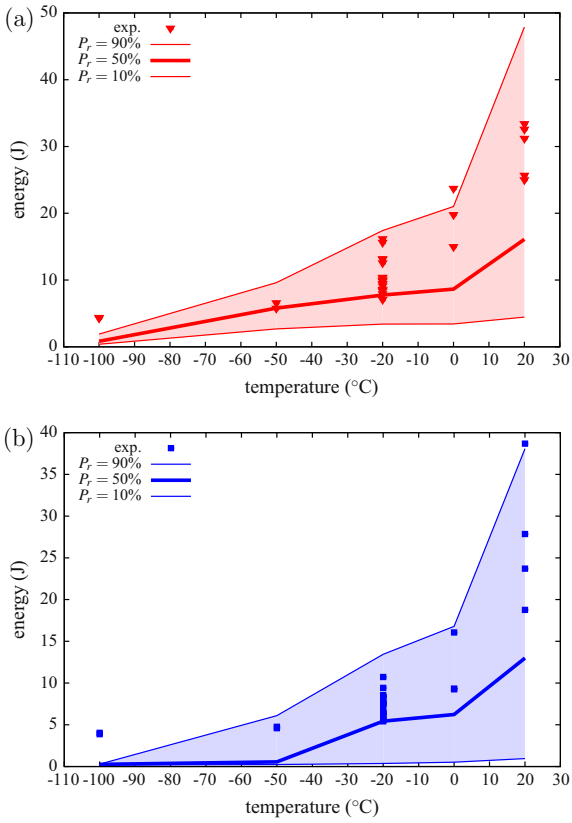

Fig. 10. Prediction of the Charpy transition curve at cleavage initiation assuming a constant value for σ_u: (a) 5% pre-strained material state and (b) 5% pre-strained + aged material state.

almost all experimental points are included inside the 10–90% fracture probability interval, even if most of them are above the 50% fracture probability curve. However, at −100 °C the model turns out to be too conservative since the numerical prediction is half that of the experimental results. Some tensile experiments at −100 °C on specimens pre-strained at 5% and prestrained at 5% + aged should be carried out in order to validate if the hypothesis made for the initial values of ρ_0 and t_{a0} remain valid at this temperature.

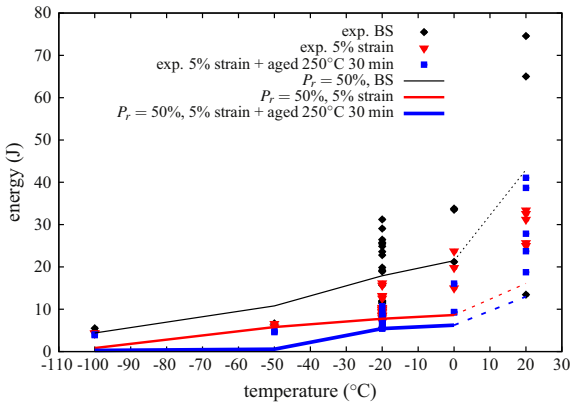

Fig. 11. Prediction of the Charpy transition curve at cleavage initiation assuming a constant value for σ_u for the three different material states, BS, 5% pre-strained and 5% pre-strained + aged material states.

A comparison of the numerically obtained fracture probability for the three states is reported in Fig. 11 that combines all the experimental and simulation results. Only the 50% probability is plotted on the figure for the sake of clarity. A shift of the lower part of the ductile-to-brittle transition is clearly observed between base state and 5% pre-strained state, and to a lesser extent between the 5% pre-strained and 5% pre-strained + aged states. These shifts are in good agreement with the ones experimentally observed in Houssin et al. [28] or in Section 2.3 (see Fig. 3).

Maps of the cumulated plastic strain in finite element simulations of Charpy impact tests at a displacement equal to 0.215 mm for the 5% pre-strained and 5% pre-strained + aged states are plotted in Fig. 12. This value of displacement is located on the force/displacement just beyond the apparent yielding, where the difference between the two curves is most pronounced. It can be seen that the localization phenomenon is much more pronounced for the 5% pre-strained + aged states than for the 5% pre-strained one.

3.5. Improved description of the pre-strained material response using kinematic hardening

According to the previous simulations, the mechanical model tends to overestimate the CVN energy compared to experimental results for the 5% pre-strained and 5% pre-strained + aged states. In this section a modification of the mechanical model is proposed in order to improve the prediction of fracture. The main idea is to investigate the effect of local non-proportional loading paths on fracture of the specimen. Indeed, the 5% pre-strained and 5% pre-strained + aged specimens are cut along the transverse direction of the sheet in a bar also pre-strained in this direction. Then just beyond the notch, the loading path remains more or less monotonic (pure tension). However beyond the striker, the loading path switches from pure tension to compression between the prestraining and the Charpy test, and is no longer proportional. In the remainder of the sample, the loading follows most likely some complex paths in the stress space.

If the assumption of a pure isotropic hardening is not verified, it can then lead to inexact results, especially if the plastic zone is large i.e. at the lower end of the ductile-to-brittle transition region. The material model was therefore modified to include kinematic hardening in addition to isotropic hardening. To estimate the balance between kinematic and isotropic hardening parts, two complex uniaxial experiments have been performed on the same type of specimens as the 5% pre-strained-aged–5% pre-strained experiments presented in Fig. 8. The first specimen was loaded at 20 °C at a prescribed strain rate of $10^{-3}\,s^{-1}$ in tension up to 5%. Then the sample was deformed in compression at the same strain rate to bring the global strain back to zero. The second specimen underwent the same cycle at 20 °C except that it was subjected to an ageing time of 30 min at 250 °C at zero force between the tensile and compression sequences. The stress vs. strain curve of these two experiments are plotted respectively in Fig. 13(a) and (b) together with the associated initial (purely isotropic hardening) and modified (combined isotropic/kinematic hardening) model responses. The experimental result of Fig. 13(a) clearly shows the strong Bauschinger effect exhibited by the material.

A kinematic hardening stress $\underset{\sim}{\boldsymbol{X}}$ is introduced in the yield function of the initial model, associated with the hardening internal variable $\underset{\sim}{\boldsymbol{\alpha}}$ (for more details see [14]):

$$f(\underset{\sim}{\boldsymbol{\sigma}}, \underset{\sim}{\boldsymbol{X}}) = J_2(\underset{\sim}{\boldsymbol{\sigma}} - \underset{\sim}{\boldsymbol{X}}) - R(\rho) - R_a(t_a) \tag{12}$$

$$\underset{\sim}{\boldsymbol{X}} = \frac{2}{3} C \underset{\sim}{\boldsymbol{\alpha}} \tag{13}$$

$$\dot{\underset{\sim}{\boldsymbol{\alpha}}} = \dot{\underset{\sim}{\boldsymbol{\varepsilon}}}_p - D\dot{p}\,\underset{\sim}{\boldsymbol{\alpha}} = \left(\underset{\sim}{\boldsymbol{n}} - D\,\underset{\sim}{\boldsymbol{\alpha}}\right)\dot{p} \tag{14}$$

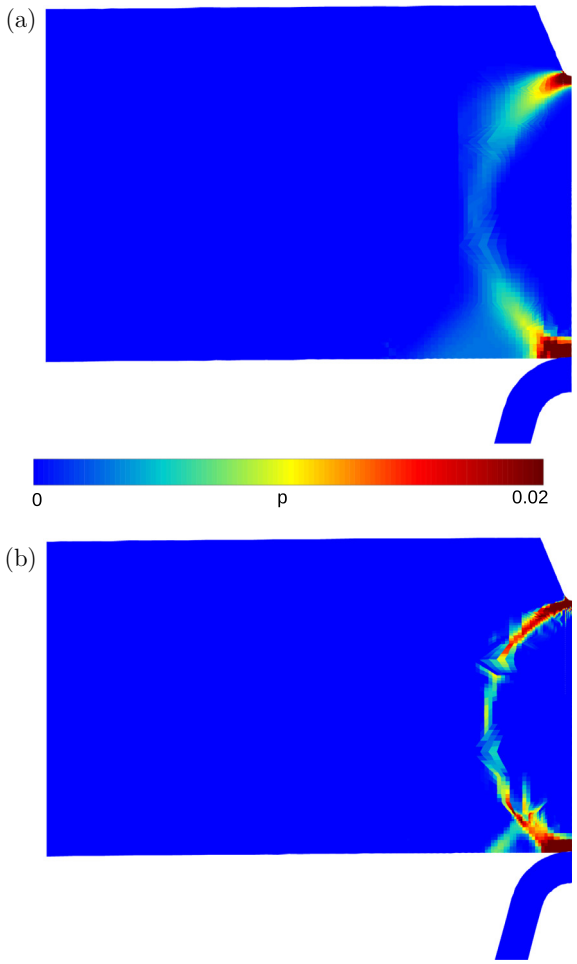

Fig. 12. Cumulated plastic strain for a displacement of 0.215 mm. (a) 5% pre-strained state and (b) 5% pre-strained + aged state.

The parameters C and D were identified from the experimental curve of Fig. 13(a) together with a modification of the parameters A and B to balance the isotropic hardening contribution with the kinematic one. The parameter σ_0 has also been modified in order to reproduce at least partially the Bauschinger effect experimentally observed. Finally the parameter P_1 is modified to correctly describe the level of the initial stress peak (for more details on the role of σ_0 and P_1 on the stress peak modeling, the interested reader should refer to Marais et al. [30]). The initial and modified values for all these parameters are given in Table 5.

It can be seen from Fig. 13(a) that the purely isotropic model fails at describing the reverse path, while using the modified one improves the description of the compressive part. The second experiment presented in Fig. 13(b) reveals another striking phenomenon already investigated in some Refs. [17,46] with dissimilar results: the existence of the Lüders stress peak and plateau after aging at zero force and reversal of the applied stress. This experiment has been repeated twice under the same conditions with very similar results. The results of Fig. 13(b) show that tension followed by aging at zero force and compression leads to a stress peak in the compression regime with a stress drop amplitude comparable to the one observed in the first tension. The strong Bauschinger effect and the higher final stress level are also observed for this loading sequence. Neither the initial model nor the modified one are able to accurately describe the reverse path for this experiment because of the overstress due to partial unpinning already observed in Fig. 8. However in order to remain consistent with the rest of the study, the modified model is used to investigate the effect of kinematic hardening introduction on prediction of the fracture of Charpy specimens.

The influence of the introduction of kinematic hardening on fracture of Charpy specimens was investigated at 20 °C, since the reverse tensile experiments were only carried out at this temperature. Five Charpy specimens were tested at 20 °C for the 5% pre-strained and the 5% pre-strained + aged states. Following the approach proposed in part Section 3.2 at the temperature of −20 °C at which fracture stress scatter was studied, the smallest CVN energy experimental values are associated with a fracture probability equal to 16.7% $(1/(1+5))$. These experimental values are compared in Table 6 with the corresponding numerical predictions provided by the initial and modified models for both states.

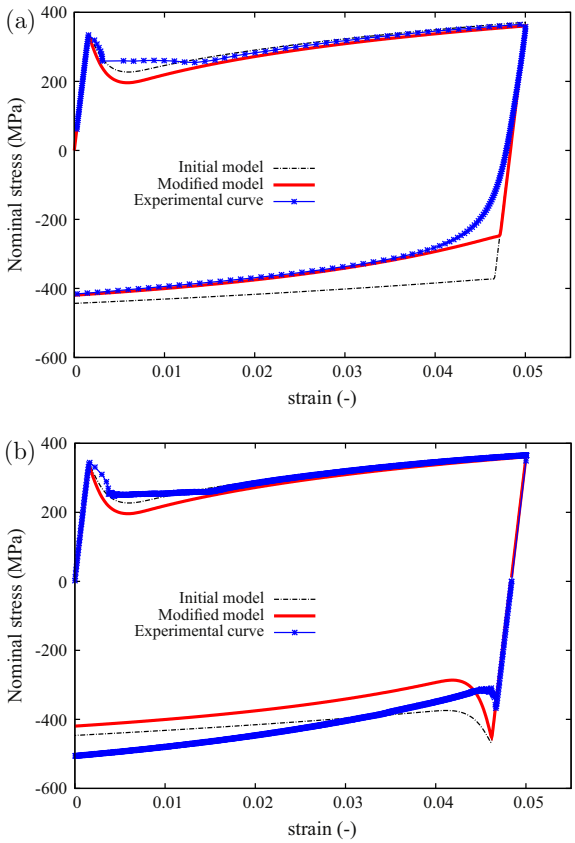

Fig. 13. (a) 5% tension–5% compression and (b) 5% tension–30 min at 250 °C–5% compression experiments at 20 °C and a prescribed strain rate of $1 \cdot e{-}3\ s^{-1}$. Comparison between the stress–strain curves generated using the initial and modified models.

Table 5
Modified and initial sets of parameters at 20 °C for non-linear isotropic and kinematic hardening.

	Modified model	Initial model
$A\ (m^{-2})$	2.15e16	3.086e16
$B\ (m^{-2})$	4.80e15	5.115e15
σ_0 (MPa)	55	130
C (MPa)	3140	×
D	49.5	×
P_1 (MPa)	350	183.2

Table 6
Experimental (5% pre-strained state, 20 °C) and numerical CVN energies for a fracture probability equal to 16.6%.

	Initial model (J)	Modified model (J)	Experimental value (J)
5% pre-strained	6.7	19.4	25
5% pre-strained + aged	4.9	5.7	18.7

As it was already observed in the previous part, the initial model tends to underestimate the CVN energies for both states. The modified model prediction for the 5% pre-strained state is more accurate by increasing the CVN energy close to the experimental value, even though at this temperature the ductile failure propagation should also be accounted for in addition to the brittle failure model. Nevertheless, at this temperature and for this state the average ductile fracture surface fraction measured on the five specimens does not exceed 35%. The brittle fracture is then still the prevailing mode. The estimation of CVN energy is significantly modified by the introduction of the kinematic hardening term. Kinematic hardening tends to "weaken" the area located close to the striker. By a structural effect, this "softening" will modify (i) the stress field beyond

the notch, (ii) the global force vs. displacement evolution; which will both be lower than using the initial model. Both effects lead to a significant increase of the predicted CVN energies given by the Beremin model.

The modified model prediction for the 5% pre-strained + aged state is less affected by the introduction of the kinematic term. Indeed the plastic zone is smaller than for the 5% pre-strained and consequently the "softening" in the area located close to the striker is less pronounced. The inclusion of kinematic hardening is then important in the prediction of accurate CVN at the lower end of the ductile-to-brittle transition region (5% pre-strained state) but less important in the very beginning of this transition (5% pre-strained + aged state).

4. Discussion and conclusion

A good agreement was found between the predicted ductile-to-brittle transition curve for the pre-strained and aged material state showing the interest of using a constitutive model including strain aging effects. The advantage of the approach is that the optimal magnitude of pre-straining and duration of heat treatments can be determined computationally in a systematic way. Zhang and McCormick's model turns out to be a simple and efficient approach to the constitutive modeling of strain aging, even though several limitations have been evidenced. In particular, the current knowledge on diffusion of solute atoms in steels in relation to dislocation densities, as discussed in Ballarin et al. [4], should be incorporated in the model to allow for a reliable simulation of heat treatments. The experimental results provided in this work confirm that the freeing of dislocations at obstacles at the yield point is generally not complete so that the stress drop remains a quantity that is difficult to predict. The model used in this work invariably leads to complete release of dislocation and maximum stress drop. Improvements require a detailed account of dislocation populations evolution in the model, like a separation into forest and mobile dislocation densities as done by Fressengeas et al. [19].

This work must be followed by efforts to address the ductile part of the ductile-to-brittle transition curve. Such an attempt can be found in Berdin and Wang [9] for uncoupled ductile damage models. Existing fully coupled ductile fracture models like Gurson and Rousselier potentials should be combined with the strain aging model by introducing the relevant internal variable t_a [50]. FE simulations of ductile tearing are usually associated with mesh dependence that can be overcome by the introduction of intrinsic length scales in the continuum model. The use of strain gradient plasticity in the context of Lüders band formation and propagation was recently examined by Mazière and Forest [33], following initial ideas by Hähner [22].

The main contributions of the present work are the following:

1. The first FE simulations of a Charpy test involving a strain aging elastoviscoplastic model were reported in this work.
2. The Beremin fracture model was identified for a nuclear C–Mn steel from a large set of experimental data including the scatter distribution at -20 °C for the base material state.
3. The prediction of the ductile-to-brittle transition curve was then possible for the pre-strained material and pre-strained and aged material states. Aging was shown to be associated with a translation of the ductile-to-brittle transition temperature towards higher temperatures.
4. The importance of kinematic hardening for an improved description of the pre-strained material's behavior was pointed out, leading to a better prediction of CVN energy at the lower end of the ductile-to-brittle transition region.
5. The existence of a Lüders peak and plateau after tension followed by unloading, aging and reverse loading was evidenced experimentally for the considered C–Mn steel.

Acknowledgements

The authors would like to acknowledge Professors A. Pineau and J. Besson for helpful discussions.

References

[1] Amar E, Pineau A. Interpretation of ductile fracture-toughness temperature-dependence of a low strength steel in terms of a local approach. Engng Fract Mech 1985;22(6):1061–71.
[2] Andrieu A, Pineau A, Besson J, Ryckelynck D, Bouaziz O. Beremin model: methodology and application to the prediction of the euro toughness data set. Engng Fract Mech 2012;95:102–17.
[3] Ballarin V, Perlade A, Lemoine X, Bouaziz O, Forest S. Mechanisms and modeling of bake-hardening steels: Part II. Complex loading paths. Metall Mater Trans A 2009;40:1375–84.
[4] Ballarin V, Soler M, Perlade A, Lemoine X, Forest S. Mechanisms and modeling of bake-hardening steels: Part I. Uniaxial tension. Metall Mater Trans A 2009;40:1367–74.
[5] Belotteau J, Berdin C, Forest S, Parrot A, Prioul C. Mechanical behavior and crack tip plasticity of strain aging sensitive steel. Mater Sci Engng A 2009;526:156–65.
[6] Benallal A. Perturbation and stability of rate-dependent solids. Eur J Mech A/Solids 2000;19:S45–60.
[7] Benallal A, Berstad T, Borvik T, Clausen A, Hopperstad S. Dynamic strain aging and related instabilities: experimental, theoretical and numerical aspects. Eur J Mech A/Solids 2006;25:397–424.
[8] Benallal A, Borvik T, Clausen A, Hopperstad O. Dynamic strain aging, negative strain-rate sensitivity and related instabilities. Tech Mech 2003;23:160–6.
[9] Berdin C, Wang H. Local approach to ductile fracture and dynamic strain aging. Int J Fract 2013;182:39–51.

[10] Beremin F. Cavity formation from inclusions in ductile fracture of A508 steel. Metall Mater Trans 1981;12(5):723–31.
[11] Beremin FM. A local criterion for cleavage fracture of a nuclear pressure vessel steel. Metall Trans A 1983;14:2277–87.
[12] Bertram A. Elasticity and plasticity of large deformations. Springer; 2005.
[13] Besson J. Local approach to fracture. Ecole des Mines de Paris–Les Presses; 2004.
[14] Besson J, Cailletaud G, Chaboche J-L, Forest S. Non linear mechanics of materials. Springer; 2009.
[15] Bordet S, Tanguy B, Besson J, Bugat S, Moinereau D, Pineau A. Cleavage fracture of RPV steel following warm pre-stressing: micromechanical analysis and interpretation through a new model. Fatigue Fract Engng Mater Struct 2006;29:799–816.
[16] Cottrell AH, Bilby BA. Dislocation theory of yielding and strain ageing of iron. Proc Phys Soc 1949;A62(1):49–62.
[17] Elliot RA, Orowan E, Udoguchi T, Argon AS. Absence of yield points in iron on strain reversal after aging, and the Bauschinger overshoot. Mech Mater 2004;36:1143–53.
[18] François F, Pineau A, Zaoui A. Mechanical behaviour of materials. Fracture mechanics and damage. Solid mechanics and its applications, vol. 191. Springer; 2013.
[19] Fressengeas C, Beaudoin A, Lebyodkin M, Kubin L, Estrin Y. Dynamic strain aging: a coupled dislocation-solute dynamic model. Mater Sci Engng 2005;A400:226–30.
[20] Graff S, Forest S, Strudel JL, Prioul C, Pilvin P, Béchade JL. Strain localization phenomena associated with static and dynamic strain ageing in notched specimens: experiments and finite element simulations. Mater Sci Engng A 2004:181–5.
[21] Graff S, Forest S, Strudel J-L, Prioul C, Pilvin P, Béchade J-L. Finite element simulations of dynamic strain ageing effects at V-notches and crack tips. Scr Mater 2005;52:1181–6.
[22] Hähner P. Modelling the spatio-temporal aspects of the Portevin–Le Chatelier effet. Mater Sci Engng A 1993;164:23–34.
[23] Hallai J, Kyriakides S. On the effect of Lüders bands on the bending of steel tubes. Part I: Experiments. Int J Solids Struct 2011;48:3275–84.
[24] Hallai J, Kyriakides S. On the effect of Lüders bands on the bending of steel tubes. Part II: Analysis. Int J Solids Struct 2011;48:3285–98.
[25] Hallai J, Kyriakides S. Underlying material response for Lüders-like instabilities. Int J Plast 2013;47:1–12.
[26] Haušild P, Berdin C, Bompard P. Prediction of cleavage fracture for a low-alloy steel in the ductile-to-brittle transition temperature range. Mater Sci Engng A 2005;391:188–97.
[27] Haušild P, Nedbal I, Berdin C, Prioul C. The influence of ductile tearing on fracture energy in the ductile-to-brittle transition temperature range. Mater Sci Engng 2002;A335:164–74.
[28] Houssin B, Slama G, Moulin P. In: Steele LE, Stahlkopf KE, editors. Assuring structural integrity of steel reactor pressure vessels. London: Applied Science Publishers; 1980. p. 57.
[29] Kubin LP, Estrin Y. The Portevin–Le Chatelier effect in deformation with constant stress rate. Acta Metall 1985;33:397–407.
[30] Marais A, Mazière M, Forest S, Parrot A, Le Delliou P. Identification of a strain-aging model accounting for Lüders behavior in a C-Mn steel. Philos Mag 2012;92(28–30):3589–617.
[31] Mazière M, Besson J, Forest S, Tanguy B, Chalons H, Vogel F. Numerical aspects in the finite element simulation of the Portevin–Le Chatelier effect. Comput Methods Appl Mech Engng 2010;199:734–54.
[32] Mazière M, Dierke H. Investigations on the Portevin Le Chatelier critical strain in an aluminum alloy. Comput Mater Sci 2012;52(1):68–72.
[33] Mazière M, Forest S. Strain gradient plasticity modeling and finite element simulation of Lüders band formation and propagation. Continuum Mech Thermodyn 2015;27(1–2):83–104.
[34] McCormick P. Theory of flow localization due to dynamic strain ageing. Acta Metall 1988;36:3061–7.
[35] Mesarovic S. Dynamic strain aging and plastic instabilities. J Mech Phys Solids 1995;43:671–700.
[36] Mudry F. Etude de la rupture ductile et de la rupture par clivage d'aciers faiblement alliés. PhD thesis, Université de Technologie de Compiègne; 1982.
[37] Mudry F. A local approach to cleavage fracture. Nucl Engng Des 1987;105:65–76.
[38] Oldfield W. Curve fitting impact test data: a statistical procedure. ASTM Stand News 1975:24–9.
[39] Pardoen T, Pineau A. Comprehensive structural integrity. In: Milne I, Ritchie RO, Karihaloo B, editors. Failure mechanisms of metals, vol. 2. Elsevier; 2007. p. 684–797 [chapter 6].
[40] Pineau A. Modeling ductile to brittle fracture transition in steels—micromechanical and physical challenges. Int J Fract 2008;150:129–56.
[41] Pineau A, Tanguy B. Advances in cleavage fracture modelling in steels: micromechanical, numerical and multiscale aspects. CR Phys 2010;11:316–25.
[42] Rittel D, Tanguy B, Pineau A, Thomas T. Impact fracture of a ferritic steel in the lower shelf regime. Int J Fract 2002;117:101–12.
[43] Rossoll A, Berdin C, Forget P, Prioul C, Marini B. Mechanical aspects of the Charpy impact test. Nucl Engng Des 1999;188:217–29.
[44] Rossoll A, Berdin C, Prioul C. Determination of the fracture toughness of a low alloy steel by instrumented Charpy impact test. Int J Fract 2002;115:205–26.
[45] Rossoll A, Tahar M, Berdin C, Piques R, Forget P, Prioul C, et al. Local approach of the Charpy test at low temperature. J Phys IV 1996;6:279–86 [EUROMECH – MECAMAT 96/1st European mechanics of materials conference on local approach to fracture 86–96, Fontainebleau, France, September 09–11, 1996].
[46] Saada G, Kruml T. Removal of plastic instabilities by reversal of the applied stress. Philos Mag 2012;93(1-3, SI):256–71.
[47] Shterenlikht A, Howard IC. The CAFE model of fracture – application to a TMCR steel. Fatigue Fract Engng Mater Struct 2006;29(9–10):770–87.
[48] Sidoroff F, Dogui A. Some issues about anisotropic elastic–plastic models at finite strain. Int J Solids Struct 2001;38:9569–78.
[49] Strnadel B, Hausild P. Statistical scatter in the fracture toughness and Charpy impact energy of pearlitic steel. Mater Sci Engng A-Struct Mater Prop Microstruct Process 2008;486(1–2):208–14.
[50] Tanguy B, Besson J. An extension of the Rousselier model to viscoplastic temperature dependent materials. Int J Fract 2002;116:81–101.
[51] Tanguy B, Besson J, Pineau A. Comment on "Effect of carbide distribution on the fracture toughness in the transition temperature region of an SA 508 steel". Scr Mater 2003;49:191–7.
[52] Tanguy B, Besson J, Piques R, Pineau A. Ductile–brittle transition of a A508 steel characterized by the Charpy impact test. Part-I: Experimental results. Engng Fract Mech 2005;72:49–72.
[53] Tanguy B, Besson J, Piques R, Pineau A. Ductile–brittle transition of a A508 steel characterized by the Charpy impact test. Part-II: Modelling of the Charpy transition curve. Engng Fract Mech 2005;72:413–34.
[54] Van den Beukel A. Theory of the effect of dynamic strain aging on mechanical properties. Phys Status Solidi a 1975;30:197.
[55] Wagner D, Moreno J, Prioul C. Influence of post weld heat treatment on the dynamic strain aging of C–Mn steels. J Phys IV 1996;6:159–62.
[56] Wagner D, Moreno J, Prioul C. Dynamic strain aging sensitivity of heat affected zones in C–Mn steels. J Nucl Mater 1998;252:257–65.
[57] Wagner D, Moreno J, Prioul C, Frund J, Houssin B. Influence of dynamic strain aging on the ductile tearing of C–Mn steels: modelling by a local approach method. J Nucl Mater 2002;300:178–91.
[58] Wang H, Berdin C, Mazière M, Forest S, Prioul C, Parrot A, et al. Portevin–Le Chatelier (PLC) instabilities and slant fracture in C–Mn steel round tensile specimens. Scr Mater 2011;64:430–3.
[59] Wang H, Berdin C, Mazière M, Forest S, Prioul C, Parrot A, et al. Experimental and numerical study of dynamic strain ageing and its relation to ductile fracture of a C–Mn steel. Mater Sci Engng A 2012;547:19–31.
[60] Wenman M. Fitting small data sets in the lower ductile-to-brittle transition region and lower shelf of ferritic steels. Engng Fract Mech 2013;98:350–64.
[61] Wenman MR, Chard-Tuckey PR. Modelling and experimental characterisation of the Lüders strain in complex loaded ferritic steel compact tension specimens. Int J Plast 2010;26:1013–28.
[62] Z-set package. Non-linear material & structure analysis suite; 2013. <www.zset-software.com>.
[63] Zhang S, McCormick P, Estrin Y. The morphology of Portevin–Le Chatelier bands: finite element simulation for Al–Mg–Si. Acta Mater 2001;49:1087–94.